2

Imaging and Display of Human Size Scenes by Long Wavelength Digital Holography

Massimiliano Locatelli[1], Eugenio Pugliese[1], Melania Paturzo[2], Vittorio Bianco[2], Andrea Finizio[2], Anna Pelagotti[1], Pasquale Poggi[1], Lisa Miccio[2], Riccardo Meucci[1] and Pietro Ferraro[2]

[1]*CNR, Istituto Nazionale di Ottica, Largo E. Fermi, Italy*
[2]*CNR, Istituto Nazionale di Ottica, Sezione di Napoli, Italy*

2.1 Introduction

This chapter is devoted to the description of *Digital Holography* (DH) [1–4] in the infrared region. As we will see, this portion of the electromagnetic spectrum offers interesting and useful opportunities for imaging purposes from various points of view. *Infrared Radiation Digital Holography* (IRDH) is an almost unexplored research field. Recently, new breakthrough potentialities of IRDH have been demonstrated, allowing us to overcome some of the most binding conditions of DH at visible wavelengths. Hence, a completely new class of products can be provided, taking advantage of the longer wavelength employed, thus involving out-of-lab applications to be exploited in the field of safety. The next sections will be devoted to showing such capabilities.

2.2 Digital Holography Principles

A hologram is the recorded interference pattern between two waves emitted by a coherent source. The wavefront impinging on the target of interest, which is scattered toward the recording device, is commonly referred to as the *object beam*, whereas the wave directly reaching the detector is the *reference beam*. Holography is a two-step process, the first step aims to record

Multi-dimensional Imaging, First Edition. Edited by Bahram Javidi, Enrique Tajahuerce and Pedro Andrés.

the hologram, and a second step whose purpose is to reconstruct the object wavefront or, as is usually said, to reconstruct the hologram [1].

In principle, any portion of the recording device can collect the information coming from each portion of the object, regardless of its size. In this configuration it is possible to use any portion, however small, of the hologram to reconstruct the entire wavefront, even though, as we will see, the smaller the portion of the hologram, the lower the final reconstruction resolution will be. In a typical holographic configuration the object beam and the reference beam travel different paths but, in order to obtain interference fringes, they must be coherent with each other and therefore, they are usually extracted from a single laser beam. For the same reason the corresponding optical paths cannot differ more than the laser coherence length. Furthermore, as in every interferometry experiment, in order to get good interference fringe visibility, the two beams should have comparable intensities and the differences between the two optical paths should be kept stable, within a fraction of the wavelength, during the time required to perform hologram recording. Finally, in order to obtain an undistorted reconstructed object wavefront, the reference beam amplitude has to be uniform across the recording device surface; strictly speaking every homogeneous reference wave could therefore be used. Usually, however, only plane waves or large curvature spherical waves are employed.

From the point of view of theory and purpose, DH is directly derived from analog holography but differs from it for the hologram recording medium and for the wavefront reconstruction method [2–10]. In DH the recording medium is a digital device, typically a CCD or a CMOS device. The interference pattern, containing the information about the wavefront to be studied, is sampled and digitized by the electronics of the device and stored in the memory of a computer as a matrix of numbers [11–19]. Hence, DH takes advantage of the joint capabilities of coherent imaging and numerical processing allowing us to obtain new products, including both qualitative imaging and quantitative phase microscopy. In this framework the capability of DH at visible wavelengths to see clearly through turbid fluids has been recently demonstrated (e.g., blood), paving the way for deep exploitation of this technique in industrial and biomedical research fields [20–22].

Current electronic recording devices, however, have a much smaller spatial resolution with respect to old photographic plates: the resolution attainable with a classic support can reach a maximum of about 7000 *cycles*/mm (where cycle means a pair of white/black fringes) while a CCD with square pixels of lateral dimensions greater than 5 μm (a typical values in CCD cameras) can solve a maximum of 100 *cycles*/mm. This limitation is particularly restrictive when working in off-axis holography where the maximum recordable number of *cycles*/mm directly imposes a limit on the angle θ between the reference beam and the normal to the sensor. If we refer, in particular, to speckle holography in optimal recording conditions, the recording device should be able to solve entirely the interference pattern resulting from the superposition of the reference wave with the waves spread by all the different points constituting the object under investigation. The maximum value of the angle θ between the reference and the object beam in off-axis configurations is thus related to the lateral dimension of the object, to the lateral dimension of the detector, and to the distance between them. If, for simplicity, we refer to the simplified bi-dimensional configuration sketched in Fig. 2.1, we can quantify these relations by means of simple geometrical considerations.

If we want all the object point sources to contribute to the interference pattern across the entire detector, it is necessary that the interference fringes between the reference beam and the highest spatial frequency component of the object wave can be recorded by the detector; if

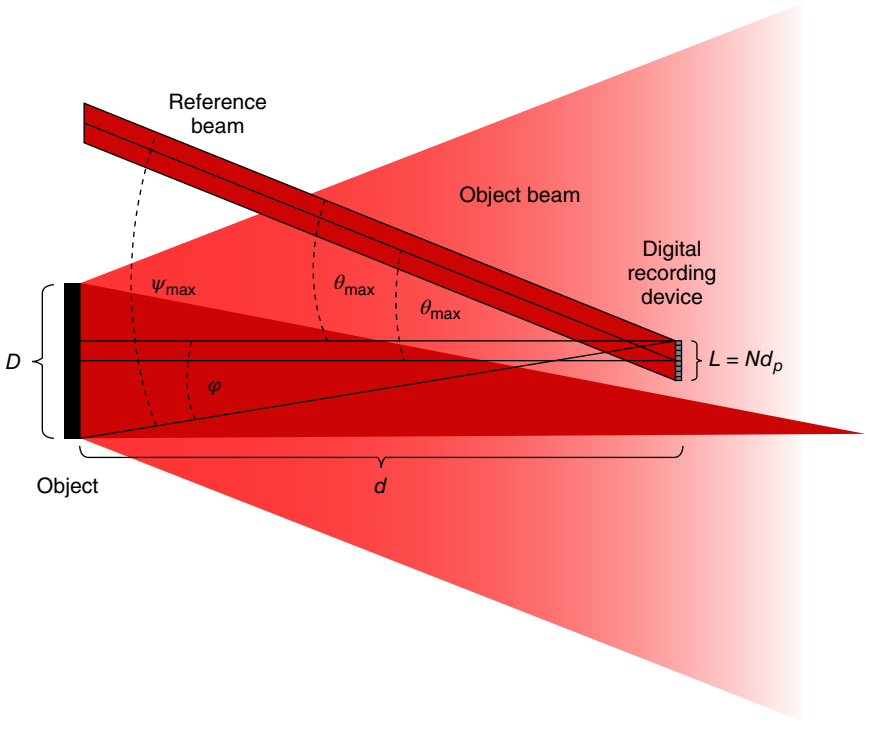

Figure 2.1 Maximum θ angle value according to the sampling condition. *Source:* M. Locatelli, E. Pugliese, M. Paturzo, V. Bianco, A. Finizio, A. Pelagotti, P. Poggi, L. Miccio, R. Meucci, and P. Ferraro 2013. Reproduced with permission from the Optical Society

we indicate with φ the angle formed by the highest spatial frequency originating in the object with respect to the detector axis, we observe [3], across the sensor, a sinusoidal interference fringe pattern between this highest spatial frequency and the reference beam with period

$$P = \frac{\lambda}{\sin\theta + \sin\varphi} = \frac{\lambda}{2\sin\left(\frac{\theta+\varphi}{2}\right)\cos\left(\frac{\theta-\varphi}{2}\right)}, \tag{2.1}$$

which, for $\theta \cong \varphi$ and $\theta + \varphi = \psi$, becomes

$$P \cong \frac{\lambda}{2\sin\left(\frac{\psi}{2}\right)}, \tag{2.2}$$

where λ is the employed wavelength. The maximum angle, ψ_{max}, allowed by Whittaker–Shannon sampling theorem is reached when the value of the fringe period reaches its minimum admitted value, P_{min}, equal to two times the detector pixel's lateral dimension d_p

$$P_{min} = \frac{\lambda}{2\sin\frac{\psi_{max}}{2}} = 2d_p \tag{2.3}$$

the maximum angle $\psi_{\max}$ thus results as

$$\psi_{\max} = 2\sin^{-1}\left(\frac{\lambda}{4d_p}\right) \overset{small\ angle}{\approx} \frac{\lambda}{2d_p}. \tag{2.4}$$

Considered the typical pixel pitch values for most used wavelengths, it follows that the small angle approximation is usually well satisfied.

With simple geometric considerations it is thus simple to calculate the maximum value $\theta_{\max}$, that is

$$\begin{aligned}\theta_{\max} = \psi_{\max} - \varphi = 2\sin^{-1}\left(\frac{\lambda}{4d_p}\right) - \tan^{-1}\left(\frac{\frac{D}{2}+\frac{L}{2}}{d}\right) \overset{small\ angle}{\approx} \frac{\lambda}{2d_p} \\ - \frac{D+L}{2d} \overset{D\gg L}{\approx} \frac{\lambda}{2d_p} - \frac{D}{2d},\end{aligned} \tag{2.5}$$

where

D = is the object lateral dimension
L = is the sensor lateral dimension
d = is the object-sensor distance.

The reconstruction of the wavefront is performed numerically by means of appropriate algorithms reproducing the diffraction process operated on the reconstruction beam by the optical transmittance constituting the hologram; it is thus possible to derive the desired information on the wavefront under investigation, both in amplitude and phase, and to reconstruct the wavefront in a digital version too [21–23].

To obtain numerically the analytical expression of such a wavefront we can exploit the Rayleigh–Sommerfeld formula [24] that, by placing the obliquity factor equal to 1 [3], can be written in this case as

$$\mathcal{E}(x_R, y_R) = \frac{1}{i\lambda}\iint_{-\infty}^{+\infty} \mathcal{R}(x_H, y_H) H(x_H, y_H) \frac{e^{i\frac{2\pi}{\lambda}\rho}}{\rho}\, dx_H dy_H, \tag{2.6}$$

where (Fig. 2.2)

$\mathcal{E}(x_R, y_R)$ is the complex wavefront in the reconstruction plane (X_R, Y_R)
$H(x_H, y_H)$ is the intensity of the interferogram in the hologram plane (X_H, Y_H)
$\mathcal{R}(x_H, y_H)$ is the wavefront reconstruction beam in the hologram plane
$\rho = \sqrt{d^2 + (x_R - x_H)^2 + (y_R - y_H)^2}$ is the distance between the generic point of the recording plane and the generic point of the reconstruction plane
d is the distance between the recording plane and the reconstruction plane.

From $\mathcal{E}(x_R, y_R)$ it is possible to extract the intensity value $I(x_R, y_R)$ and the phase value $\phi(x_R, y_R)$ of the object wavefront in the reconstruction plane

$$I(x_R, y_R) = \mathcal{E}(x_R, y_R)\, \mathcal{E}^*(x_R, y_R) \tag{2.7}$$

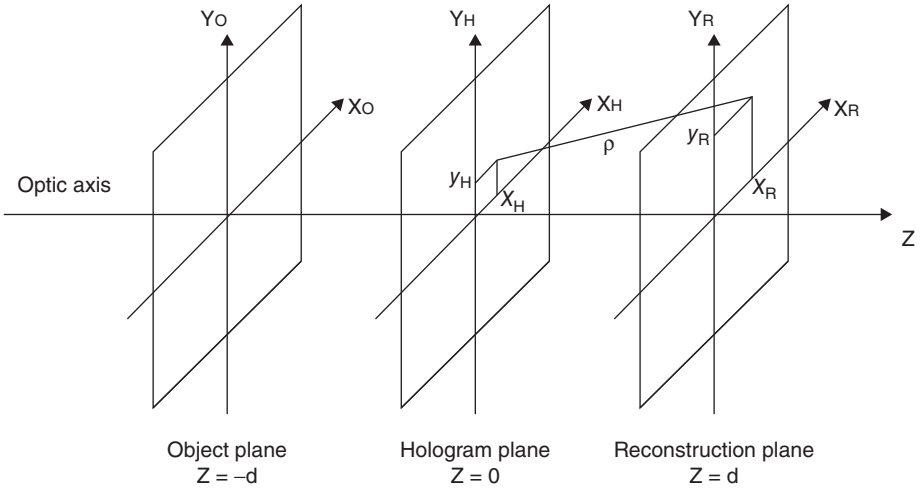

Figure 2.2 Object plane, hologram plane, and reconstruction plane. *Source:* Pelagotti A., Locatelli M., Geltrude A., Poggi P., Meucci R., Paturzo M., Miccio L., Ferraro P. 2010. Reproduced with permission from Springer

and

$$\phi(x_R, y_R) = \tan^{-1}\left(\frac{Im\left\{\mathcal{E}\left(x_R, y_R\right)\right\}}{Re\{\mathcal{E}(x_R, y_R)\}}\right). \tag{2.8}$$

A common way to operate this transformation, that is, to simulate the wavefront propagation from the recording plane to the reconstruction plane, is to follow the so-called *Fresnel method*.

2.2.1 Fresnel Method

For values of x_R, y_R, x_H, y_H small compared to the distance d between the reconstruction plane and the hologram plane, the expression of ρ can be approximated with its Taylor development

$$\rho \approx d + \frac{\left(x_R - x_H\right)^2}{2d} + \frac{\left(y_R - y_H\right)^2}{2d} - \frac{\left[\left(x_R - x_H\right)^2 + \left(y_R - y_H\right)^2\right]^2}{8d^3} + \ldots \tag{2.9}$$

The fourth term of this expression can be neglected if it is small compared to the wavelength [6], that is, if

$$\frac{\left[\left(x_R - x_H\right)^2 + \left(y_R - y_H\right)^2\right]^2}{8d^3} \ll \lambda \quad \rightarrow \quad d \gg \sqrt[3]{\frac{\left[\left(x_R - x_H\right)^2 + \left(y_R - y_H\right)^2\right]^2}{8\lambda}}. \tag{2.10}$$

Therefore, if we use the expression of the development up to the first order for the numerator (most critical factor) and up to the zero order term for the denominator (less critical factor) [4], we obtain

$$\mathcal{E}\left(x_R, y_R\right) = \frac{e^{i\frac{2\pi}{\lambda}d}}{i\lambda d} e^{\frac{i\pi}{\lambda d}\left(x_R^2+y_R^2\right)} \iint_{-\infty}^{+\infty} \mathcal{R}\left(x_H, y_H\right) H\left(x_H, y_H\right) e^{\frac{i\pi}{\lambda d}\left(x_H^2+y_H^2\right)} e^{\frac{i2\pi}{\lambda d}\left(-x_H x_R - y_H y_R\right)} dx_H dy_H. \tag{2.11}$$

This equation is called the Fresnel approximation of the Rayleigh–Sommerfeld integral or *Fresnel transform*. If we now define the variables

$$\mu = \frac{x_R}{\lambda d}, \qquad \nu = \frac{y_R}{\lambda d} \tag{2.12}$$

the previous integral becomes

$$\mathcal{E}\left(\mu, \nu\right) = \frac{e^{i\frac{2\pi}{\lambda}d}}{i\lambda d} e^{i\pi\lambda d\left(\mu^2+\nu^2\right)} \iint_{-\infty}^{+\infty} \mathcal{R}\left(x_H, y_H\right) H\left(x_H, y_H\right) e^{\frac{i\pi}{\lambda d}\left(x_H^2+y_H^2\right)} e^{-i2\pi\left(x_H\mu + y_H\nu\right)} dx_H dy_H. \tag{2.13}$$

The expression, in this way, has thus assumed, unless the multiplication factor out of the integral not depending on the variables x_H, y_H, the appearance of a two-dimensional Fourier transform and we can therefore write

$$\mathcal{E}\left(\mu, \nu\right) = \frac{e^{i\frac{2\pi}{\lambda}d}}{i\lambda d} e^{i\pi\lambda d\left(\mu^2+\nu^2\right)} \mathcal{F}\left\{\mathcal{R}\left(x_H, y_H\right) H\left(x_H, y_H\right) e^{\frac{i\pi}{\lambda d}\left(x_H^2+y_H^2\right)}\right\}, \tag{2.14}$$

where $\mathcal{F}$ denotes the Fourier transform.

It should be recalled, at this point, that in digital holography, hologram recording is performed in the digital domain and $H(x_H, y_H)$ is therefore a discretized function; if we assume that the sensor is composed of a rectangular array of M by N pixels with spacing, along the axes X_H and Y_H, respectively equal to Δx_H and Δy_H, our hologram appears to be an array of numbers $H(k\Delta x_{\mathrm{H}}, l\Delta y_{\mathrm{H}}) = H(k, l)$ and the previous integrals are therefore to be transformed into discrete summations or, equivalently, the continuous Fourier transform has to be replaced by a discrete Fourier transform; the wavefront on the reconstruction plane is then, in turn, a discrete function $\mathcal{E}(m\Delta\mu, n\Delta\nu) = \mathcal{E}(m, n)$ of the discrete variables $m\Delta\mu$, $n\Delta\nu$; taking into account that the maximum spatial frequency is determined by the sampling range in the spatial domain and namely [3]

$$\mathrm{M}\Delta\mu = \frac{1}{\Delta x_{\mathrm{H}}} \quad , \quad N\Delta\nu = \frac{1}{\Delta y_{\mathrm{H}}}. \tag{2.15}$$

It is possible to write

$$\mathcal{E}(m,n) = \frac{e^{i\frac{2\pi}{\lambda}d}}{i\lambda d} e^{i\pi\lambda d\left[\frac{m^2}{M^2\Delta x_{\mathrm{H}}{}^2}+\frac{n^2}{N^2\Delta y_{\mathrm{H}}{}^2}\right]} \mathcal{DF}\left\{\mathcal{R}(k,l)\,H(k,l)\,e^{\frac{i\pi}{\lambda d}\left[(k\Delta x_{\mathrm{H}})^2+(l\Delta y_{\mathrm{H}})^2\right]}\right\}, \quad (2.16)$$

where $\mathcal{DF}$ denotes the discrete Fourier transform.

Finally, it can be observed that, according to the Fourier transform relationship,

$$\Delta x_R = \frac{\lambda d}{M\Delta x_H}, \qquad \Delta y_R = \frac{\lambda d}{N\Delta y_H} \quad (2.17)$$

and this means that the reconstructed wavefront in the plane (X_R, Y_R), is represented by a matrix consisting of $M \times N$ elements, each of which is called reconstruction pixel, with dimensions Δx_R, Δy_R. Suppose we have a square detector ($M = N$), with square pixels ($\Delta x_H = \Delta y_H = d_p$), we have

$$\Delta x_R = \Delta y_R = d_{pr} = \frac{\lambda d}{N d_p}. \quad (2.18)$$

From these expressions it follows that the reconstruction resolution increases when the distance d decreases; unfortunately this distance cannot be reduced indefinitely because there will be a minimum value $d_{\min}$ for which the maximum angle $\theta_{\max}$ admitted by the sampling theorem coincides with the minimum value of the angle $\theta_{\min}$ required to have the diffraction orders separation; in this condition, sketched in Fig. 2.3, we thus have the maximum resolution for a certain object dimension; working at the minimum distance we thus have

$$\theta = \theta_{\max} = \theta_{\min} = \varphi = \frac{\psi_{\max}}{2} \quad (2.19)$$

and, consequently

$$\frac{\lambda}{4d_p} = \frac{D+L}{2d_{\min}} \quad \rightarrow \quad d_{\min} = \frac{2d_p(D+L)}{\lambda} \overset{D\gg L}{\approx} \frac{2d_pD}{\lambda}. \quad (2.20)$$

If we work at the minimum distance the reconstruction pixel pitch becomes

$$d_{pr} = \frac{2(D+L)}{N} = \frac{2D}{N} + 2d_p \overset{D\gg L}{\approx} \frac{2D}{N}. \quad (2.21)$$

This means that, at the minimum distance allowed by the sampling theorem, the reconstruction pixel pitch does not depend on the wavelength used to irradiate the object and cannot be smaller than twice the detector pixel pitch. Furthermore, if a large sized object, with respect to the detector lateral dimension, is investigated the reconstruction resolution increases with the number of elements constituting the detector.

2.2.2 Advantages of Digital Holography

DH is characterized by a series of interesting features that make it more appealing with respect to its classical counterpart and to most standard imaging techniques. The key feature that differentiates DH from standard imaging techniques is the possibility to reconstruct both the

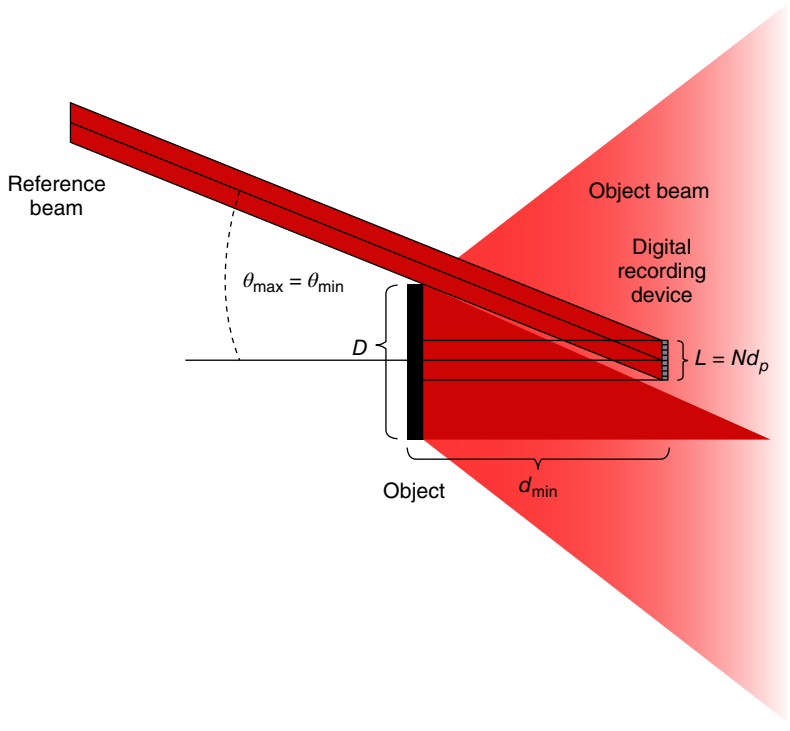

Figure 2.3 Minimum distance configuration. *Source:* Pelagotti A., Paturzo M., Geltrude A., Locatelli M., Meucci R., Poggi P., and Ferraro P., 2010. Reproduced with permission from Springer

amplitude images and the phase-contrast maps of the sample under investigation. Hence, DH allows us to perform quantitative phase microscopy of transparent samples with a label-free approach. The phase information, of great interest in a wide variety of applications, is obtained with a minimally invasive technique since the remarkable sensitivity, which characterizes modern recording digital devices allows us, if necessary, to use very low power laser radiation during the hologram recording process. Another interesting capability of DH is the possibility to perform, with a single acquisition, the reconstruction of the object image at different distances; this means that tunable focusing on particulars belonging to different planes that make up the scene can be obtained numerically during the reconstruction process starting from a single recorded hologram. Furthermore, as in classical holography, each portion of a hologram carries the information of the entire sample and can be used to retrieve it; this means that even if part of the sensor is covered during the recording process it is still possible to recover the information about the entire scene under investigation. The most important advantage of DH with respect to analog holography is that the digital hologram recording process is by far faster and easier than its analog counterpart: no delicate and time consuming photographic recording and development processes are required. Moreover, the times required for numerical reconstruction are, today, with modern computers, in the order of a second and so they do not represent a limitation in most applications.

2.3 Infrared Digital Holography

The idea behind holography is so general and rich in application that it is of interest in all regions of the electromagnetic spectrum. Obviously, the different wavelengths require different recording devices and the inhomogeneous technological development of the various acquisition devices has inevitably benefited certain regions of the spectrum with respect to others. In DH, for example, infrared (IR) sources were penalized, compared to visible sources, due to the critical issues related to the detection of this kind of radiation. However, increasing interest toward standard IR imaging techniques, firstly related to their military, industrial, and thermal efficiency applications has boosted the production of thermographic cameras and the availability of such IR cameras, based on the latest sensors generation, represents a significant stimulus to the development of DH techniques also in this region of the electromagnetic spectrum. This renewed interest could lead to innovative applications in security screening, night vision, and biological science, as it can extend holographic 3D imaging capabilities from visible light to the IR spectrum, up to the terahertz frequencies.

The advantages using long wavelength radiation to perform DH are related to some intrinsic characteristics of this technique. First of all, as we have seen in the previous paragraph, the radiation wavelength does not enter into the expression for the reconstruction pixel pitch when operating at the minimum distance admitted by the sampling theorem; the reason for this unexpected property resides in the fact that, according to the general expression of the reconstruction resolution, the longer the wavelength in use the larger the reconstruction pixel size should be (the worse the resolution) but, if we look at the expression of the maximum angle between object beam and reference beam, we see that a longer wavelength allows us to work at lower object-camera distances thus compensating for what was lost in terms of resolution. The reconstruction pixel pitch is indeed rather heavily dependent on the number and size of the elements constituting the recording device. In the past, infrared detectors were characterized by a number of sensitive elements much lower than the detectors in the visible range and, at the same time, the size of the sensing elements was much larger than those of typical CCDs. This deficiency in IR detection devices, combined with the ease of use of visible radiation, in the past prevented a significant development of DH techniques at these wavelengths. Today a typical high-level commercial uncooled mid-IR detector can have 1024×768 elements with a 20 μm lateral dimension, a typical high-level commercial visible camera can have 2048×2048 elements with 6.5 μm lateral dimension. With the expected progress of IR detection technologies, it is reasonable to assume that these values are going to be soon overcome so that the resolution gaps between visible detectors and IR detectors are intended to get smaller and smaller. Considering these typical sensors' technical values it is simple to evaluate advantages and disadvantages of *Infrared Digital Holography* (IRDH) with respect to visible DH: inserting the appropriate values in the equations for the minimum distance and for the reconstruction pixel pitch, for a fixed object dimension, D, it follows that IR radiation is the best choice if large objects are of interest, even if a slightly lower resolution is obtained. An object with 1-m lateral dimension, for example, must be at least 24 m away from a visible detector (when working at 0.632 μm) while it could stay at about 3 m if CO_2 radiation is used and even less than 0.5 m when working in the terahertz region at 100 μm. The reconstruction resolution instead maintains the same order in all cases.

There is also, however, an intrinsic advantage in using long IR radiation in DH, and more generally, in every interferometric experiment; that is, the inherent lower sensitivity to vibrations

of long wavelength radiation. In fact, in the case of optical path variations due to seismic noise or any other vibration source, the longer the wavelength is that is used to create the interference pattern, the lower the phase variation between the reference and object beams. This benefit makes the stability of the object and of the measuring apparatus in general a less critical factor during hologram acquisition and is thus strongly indicated for DH, particularly in the investigation of large objects. IR radiation thus makes it possible to work in less restrictive conditions, giving much more versatility to the technique and opening the way to many possible out-of-laboratory applications. By means of long wavelength radiation it is possible to create video holograms (meaning holographic video of slowly changing dynamical scenes) without using a pulsed laser and the short acquisition times necessary when working with visible radiation. When analysis of very large sized samples is needed, CO_2 laser radiation is strongly recommended since the high output power that CO_2 lasers can reach is required to efficiently irradiate large object surfaces. Furthermore, the very high coherence length typical of CO_2 lasers represents an important advantage in every interferometric application. All these features make CO_2 lasers highly recommended in DH applications aiming to investigate large sized objects in out-of-laboratory applications.

Among the reasons that may encourage the use of IR in DH, there is also the transparency of various materials at certain wavelengths in the IR spectrum; this property could be exploited to study internal structures of such materials at different depths, to investigate heterogeneous materials or in security and safety applications. As we will see mid-IR radiation transmits well through smoke, while far-IR is well known for its capability of passing through plastic materials, clothes, paper, wood, and many other materials. Unfortunately water is strongly absorbing both at 10.6 µm and in the terahertz region and, consequently, the exploitation of these wavelengths for biological purposes is restricted to thin sample investigation.

2.4 Latest Achievements in IRDH

In this section we will show some of the more recent and promising results obtained in the field of IRDH.

The very first results in this field were obtained in 2003 [25] employing a holographic setup in transmission configuration, using a CO_2 laser at 10.6 µm with 190 mW power and a pyroelectric camera, Pyrocam III by Spiricon, with 124 × 124 LiTaO3 elements of pixel size 85 µm × 85 µm and center to center spacing of 100 µm × 100 µm. In this first experiment the wavefront transmitted through a small drilled metallic plate was recorded and numerically reconstructed both in amplitude and phase.

The first speckle IRDH results on large size samples were obtained in 2010 [2627] using a larger size and more sensitive detector, the microbolometer detector Miricle 307 K with 640 × 480 ASi pixels at 25 µm pixel pitch; in order to guarantee a more efficient object irradiation a $100W$ CO_2 laser source and the experimental setup shown in Fig. 2.4 were employed. This is a standard holographic setup and all the experiments shown in the following sections are based on this basic configuration.

In this setup the CO_2 laser beam was first divided by a ZnSe beam splitter (BS1), which reflected 80% of the impinging radiation and transmitted the remaining 20%. The transmitted part, which constituted the reference beam, was reflected by means of a plane mirror (M1) toward a ZnSe variable attenuator (VA); the reference beam was then redirected by means of another two plane mirrors (M2, M3) toward the thermocamera but, before impinging on the

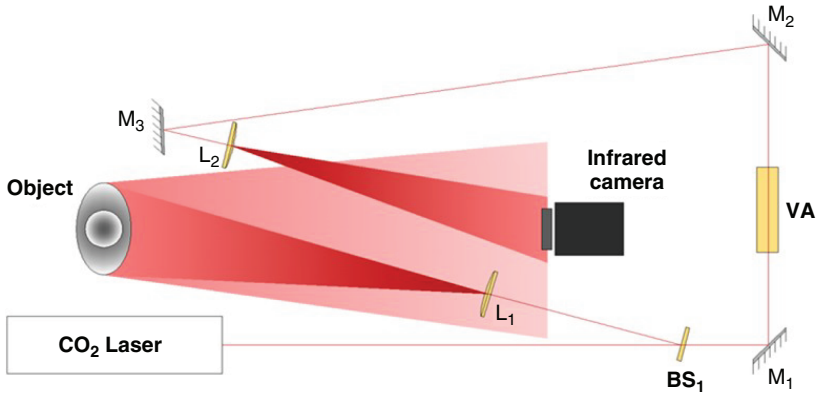

Figure 2.4 M1, M2, and M3 are plane mirrors; BS1 is a ZnSe 80/20 beam splitter; L1 and L2 are ZnSe 1.5 inch focal length spherical lenses. *Source:* Pelagotti A., Paturzo M., Locatelli M., Geltrude A., Meucci R., Finizio A., Ferraro P. 2012. Reproduced with permission from the Optical Society

detector, it encountered a ZnSe converging lens of 1.5 inch focal length (L2), which enlarged it in order to reach the thermocamera with enough low intensity and an almost planar wavefront. The reflected part of the fundamental beam indeed constituted the object beam; before impinging on the sample it passed through a ZnSe converging lens of 1.5 inch focal length (L1), which enlarged the beam so as to irradiate a fairly large surface area of the object depending on its distance from the sample. The interference pattern across the sensor was optimized in order to increase the fringe visibility, acting on the reference beam intensity by means of the variable attenuator. The hologram could be collected and digitally stored in a computer both in the form of a single image and in the form of a video if a dynamical scene was of interest. Thanks to the low sensitivity to vibration of the whole system the anti-vibration modality of the table was not activated during the experiments. Since the detector was only sensitive to IR radiation, artificial light and sunlight were not disruptive.

In Fig. 2.5 the hologram of a small bronze statue (about 10 cm high) reproducing Emperor Augustus, recorded with this configuration and its amplitude reconstruction, are shown. A second and larger size statuette (34 cm high) reproducing Benvenuto Cellini's Perseus sculpture was successfully investigated with the same configuration; in Fig. 2.6 a photo of the statue, the relative hologram, and the reconstructed amplitude wavefront are shown.

2.4.1 Super Resolution by Means of Synthetic Aperture

Since IR detector elements are larger and less numerous than typical visible detector elements, these first results lacked resolution compared to typical visible holograms. Since the hologram dimension (that is the detector surface) enters at the denominator in the reconstruction pixel pitch expression, and since the detector surface is, in general, significantly smaller than the interferometric pattern surface created in air by the object beam and the reference beam, it is possible to synthetically increase the numerical aperture of the system by means of an automatic technique capable of recording several shifted but partially superimposable holograms and stitching them together [28]. In order to collect the various holograms, the

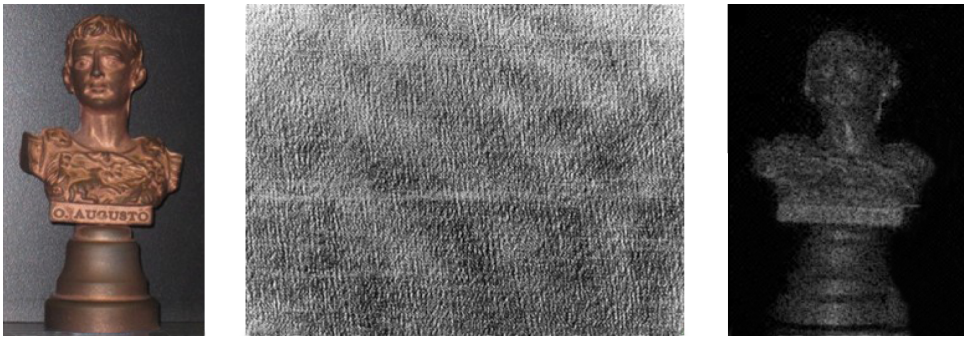

Figure 2.5 (From left to right) small statue of Augustus; IR hologram of Augustus; numerically reconstructed hologram of Augustus. *Source:* Paturzo M., Pelagotti A., Finizio A., Miccio L., Locatelli M., Geltrude A., Poggi P., Meucci R., Ferraro P. 2010. Reproduced with permission from the Optical Society

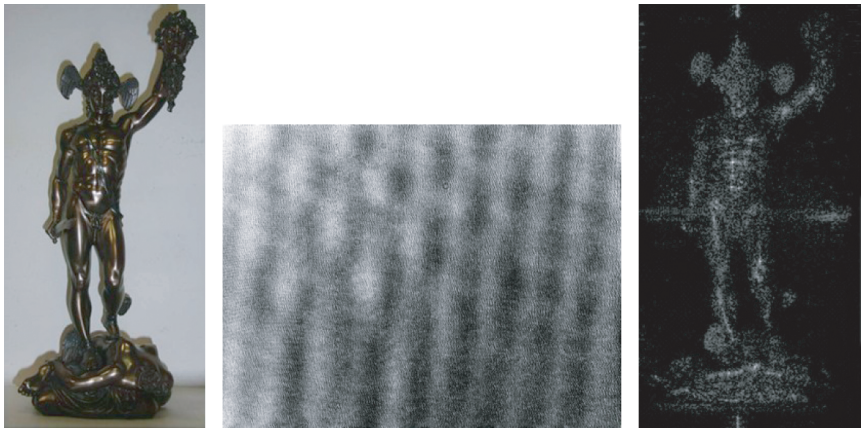

Figure 2.6 (From left to right) statue of Perseus; IR hologram of Perseus; numerically reconstructed hologram of Perseus

basic setup described in the previous section was employed but the thermocamera was fixed at two motorized translational stages; by means of a remotely controlled routine, the sensor was moved horizontally and vertically along a serpentine path on the hologram plane and acquired various equally spaced, minimally overlapping, portions of the large interferometric pattern. The recording session had to be completed in a relatively short time so as to minimize changes in the interferential pattern, even if the task was facilitated by the low vibration sensitivity of long wavelength radiation. The numerous holograms recorded were then stitched together by means of an automated algorithm, obtaining a digital hologram with a synthetic but larger numerical aperture. The stitching procedure, called *registration*, is a standard image processing technique for determining the geometrical transformation that aligns points in one picture with corresponding points in another picture. Often, registration is performed manually

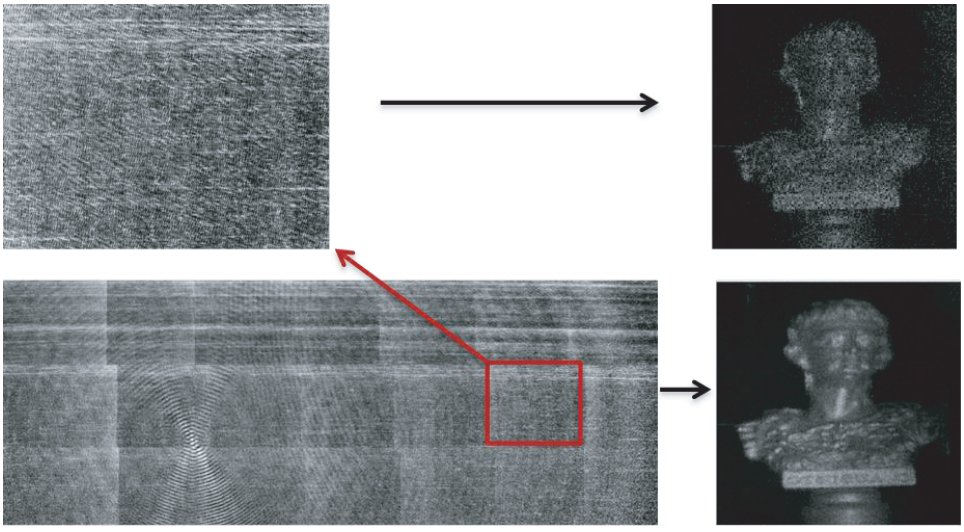

Figure 2.7 Augustus hologram stitching. (From left to right) Single hologram and single hologram amplitude reconstruction: 7×3 stitched holograms and stitched hologram amplitude reconstruction

or in a semi-automatic way by a user iteratively setting the parameters of the geometrical transformation. However, this approach is time consuming and can give subjective results. On the other sides most totally automated algorithms are not always applicable to aligning and stitching speckle holograms, which, due to their apparently random and very fine pattern, and to the inevitable inherent differences between images' structures and tones, are hard to match and experimentally result in noisy images. In this experiment a specific automated method based on the maximization of the mutual information (MMI) [29] was employed; this method was capable of taking into account any possible shift, rotation, and scaling among the different holograms, and showed excellent results compared to standard methods. With this technique it was thus possible to improve the reconstruction resolution of the previously investigated sample, the Augustus statue. In particular, a synthetic hologram composed of 7×3 standard holograms was employed to obtain the synthetic hologram and the corresponding super-resolved amplitude reconstruction of the Augustus image. The remarkable result obtained with this technique is shown in Fig. 2.7.

Again, the high power of the CO_2 laser employed in the experiment proved an advantageous parameter helping to obtain a larger interferential pattern with respect to the standard visible pattern, and therefore allowing us to acquire a larger number of single holograms for stitching together. The reconstructed image resolution, however, cannot increase indefinitely because when the synthetic aperture hologram reaches a certain dimension the reconstructed wavefront curvature, corresponding to different perspectives, cannot be properly represented with a 2D numerical reconstruction.

Noteworthy, the enhanced resolution makes it possible to exploit more efficiently the capability, peculiar to DH, to focus on different object planes: thanks to the increased numerical aperture of the synthetic hologram, the depth of focus is decreased and it becomes possible to

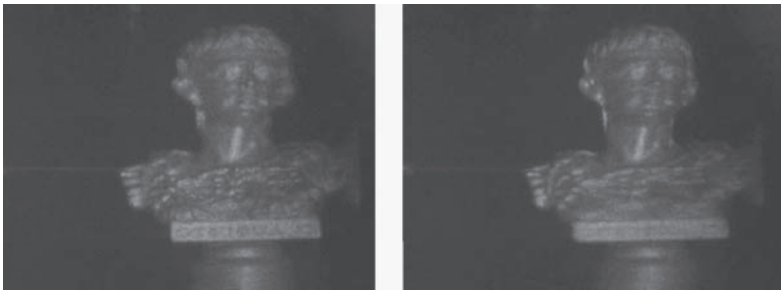

Figure 2.8 Stitched Augustus hologram amplitude reconstruction with the Augustus inscription in focus (on the left) and with Augustus' head in focus (on the right)

read the inscription on the base of the Augustus statue in the reconstructed image (left image of Fig. 2.8), or to focus on Augustus' head (right image of Fig. 2.8), simply by changing the numerical reconstruction distance.

2.4.2 Human Size Holograms

As we have already mentioned, by means of long wavelength DH, it is possible to obtain advantages in terms of a larger field of view and lower sensitivity to seismic noise. Furthermore, using a high power source like a CO_2 laser, it is possible to irradiate quite uniformly very large surfaces. With long wavelength radiation it becomes possible to record holograms in critical conditions including illuminated environments and not ground isolated setups. Moreover, at this wavelength, holographic videos of moving objects, although at limited speed, can be easily recorded and reconstructed. All these features are fundamental if holograms of large targets are to be recorded. However, one of the peculiar difficulties in recording a digital hologram of a large object is effectively irradiating the entire surface of the sample. In order to obtain the optimal homogeneous irradiation of the target, different configurations were tested to record human size holograms [30] and, what is even more interesting, to record live person holograms [31]. In order to compare the results obtained with each configuration, the object, a plastic mannequin 1.90 cm high (Fig. 2.9 (Plate 3), was always maintained in the same position with respect to the thermocamera. In particular, the distance between the object and the thermocamera was the minimum distance for recording holograms of that size according to the equations discussed earlier.

In order to obtain a larger beam size across the sample, a high focusing lens to enlarge the object beam was employed in the basic holographic setup. This configuration, however, showed important disadvantages: since the peripheral part of the Gaussian object beam is characterized by a lower intensity, the object surface was not uniformly irradiated and this resulted in a poor and inhomogeneous reconstruction quality of the outer part of the sample. Furthermore, the object beam dimension was limited by the focusing power of the lens and, consequentially, only a portion of the sample could be fruitfully irradiated. In these conditions we could not take complete advantage of the increased field of view offered by the longer wavelength because the irradiated area was smaller than the maximum

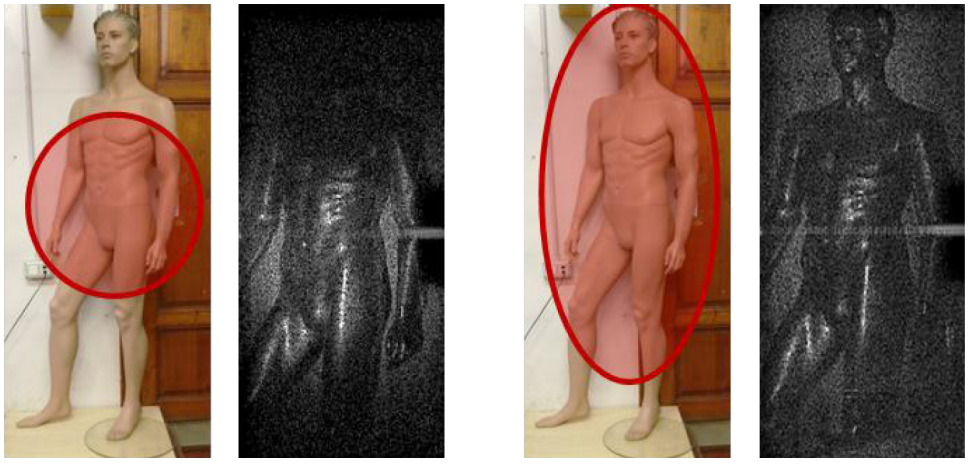

Figure 2.9 (Plate 3) (a) Spherical lens configuration. Mannequin image with irradiated area in red; mannequin hologram amplitude reconstruction. (b) Cylindrical lens configuration. Mannequin image with irradiated area in red; mannequin hologram amplitude reconstruction. *See plate section for the color version*

recordable size (Fig. 2.9a). When the analysis of targets extending in a preferential direction, like the human-size mannequin, is needed a cylindrical lens can be fruitfully employed to obtain a stretched beam (Fig. 2.9b). In another configuration, based on a completely different approach, the object beam, expanded by the usual spherical lens was moved along the sample, changing its propagation direction by means of a plane mirror driven by two motion control devices. Using this configuration it was thus possible to uniformly irradiate an overall surface of more than 4 m^2, an area larger than the allowed field of view.

In this case, a video hologram during which the object beam entirely scanned the mannequin surface was recorded in about half a minute. When faster scanning acquisitions are realized, the fringe visibility decreases progressively and the reconstruction resolution gradually reduces; this problem could be solved by means of a higher frame rate and a shorter exposure time. Such an acquisition procedure can be exploited in different ways: the video hologram can be reconstructed as a video that can be reproduced at normal velocity showing a slow scan of the sample, or it can be decimated and played at incremented speed so that the amplitude image of the whole object is perceived all at once; a third possibility consists of extracting the most significant frames and obtaining the whole image by their superposition as shown in Fig. 2.10 (Plate 4).

The natural following step was to test the possibility of acquiring live human holograms [31]; using the first configuration a human half bust was clearly recorded and reconstructed as shown in Fig. 2.11. Clearly, when operating with human beings, resolution gets worse because of body micro movements, and because of the lower reflectivity of human skin and clothes compared to the plastic surface of the mannequin. It is, however, important to point out that such a result would be very difficult, if not impossible, to reach with a CW visible laser in unisolated conditions.

Figure 2.10 (Plate 4) (From left to right) Mannequin image with irradiated area in red; mannequin hologram amplitude reconstruction at different scanning time and superposition of the most significant frames. *See plate section for the color version*

Figure 2.11 Amplitude reconstructions of a human half bust

2.4.3 Visible Analog Reconstruction of IR Digital Holograms

Hologram reconstruction in DH is usually implemented by means of numerical algorithms but nothing precludes to "write", somehow, the hologram on an appropriate medium in order to perform an analog reconstruction. Spatial light modulators (SLM) (arrays of pixels where each

pixel modulates the phase and the amplitude of the light transmitted through or reflected from it) are the preferred devices to accomplish this particular task [32,33]. However, in general, the SLM pixel pitch differs from the pixel pitch of the employed recording device and, furthermore, an optical reconstruction makes sense only if visible light is used, different from the case we are dealing with. The so-called *imaging equations* [3,4] relate the coordinate of an object point with that of the corresponding point in the reconstructed holographic image, in most general conditions (i.e., for a rescaled hologram and for different recording/reconstruction wavelengths). Generally, when a 3D hologram reconstruction with a different wavelength is performed, the resulting image is affected by aberrations (e.g., spherical aberration, coma, astigmatism, field curvature, and distortion). The expression of these various aberrations can be deduced from the imaging equations and it can be demonstrated [34] that if the detector-object distance is equal to the distance between the detector and the reference beam origin (i.e., in the so-called lensless Fourier holography configuration), aberrations are minimized.

In an early work [35], holograms with 10.6 μm laser source of Perseus statuette were recorded in the basic holographic arrangement but in a lensless Fourier holography configuration. In particular, 120 holograms were acquired while rotating, each time, 3° of the figurine around itself. In the reconstruction process, a diode pumped solid state laser emitting at 0.532 μm was used. The laser beam was optically manipulated so to obtain a converging beam impinging on a reflective liquid crystal on silicon (LCoS) phase only SLM (PLUTO by Holoeye with 1920×1080 pixels, 8 μm pixel pitch, and 60 Hz frame rate). The acquired holograms were played back in sequence with regular frequency. With such an arrangement it was possible to obtain an analog reconstructed movie of the rotating figurine on a screen at a fixed distance from the SLM. An image of the optically reconstructed wavefront, acquired by means of a standard CCD camera, is compared with a standard IR numerical reconstruction image in Fig. 2.12.

The experimental reconstructed image position and its magnification with respect to the real object were in good agreement with the predicted theoretical values and no significant aberration was observed.

In a later work [36], a holographic digital video display of a 3D ghostlike image of multi-view recorded holograms of Perseus, floating in space, was obtained. To achieve this result a holographic video display system built from nine LCoS phase-only SLMs (Holoeye HEO-1080P with 1920×1080 pixels, 8 μm pixel pitch, and 60 Hz frame rate) forming a circular configuration, was used (Fig. 2.13). Removal of the gaps between the SLMs was provided by a beam splitter to tile them side by side [37] and to achieve a virtual alignment with a continuous increased field of view. In order to position the reconstructed 3D image slightly above the display setup and to avoid blocking of the observer's vision by the display components, the SLMs were also tilted up at a small angle. Negligible reduction in the quality of the reconstructions for a tilted illumination of up to 20° has been shown by experiments [36]. All SLMs were illuminated with a single astigmatic expanding wave by means of a cone mirror as shown in Fig. 2.13. With the help of this configuration, observers can see the 3D ghost-like image floating in space and can move and rotate it around (Fig. 2.14). These two works demonstrate the possibility of obtaining direct real-time 3D vision of IR-recorded digital holograms and, considering the previously underlined capability of IRDH to investigate large size samples, emphasize the potentialities of IRDH as a valuable candidate in the research field of real 3D TV and for possible virtual museum applications.

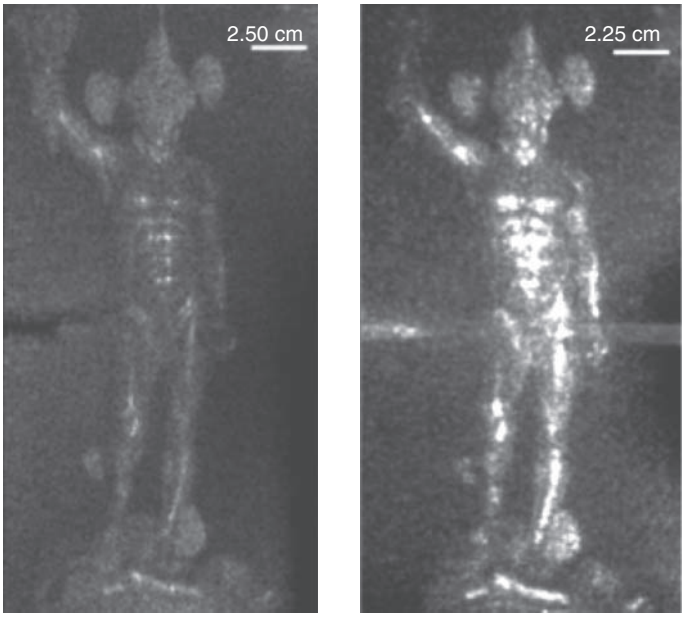

Figure 2.12 (a) Numerical reconstruction of Perseus statuette hologram. (b) SLM optical reconstruction of Perseus statuette hologram performed at a visible wavelength and collected by a monochromatic CCD

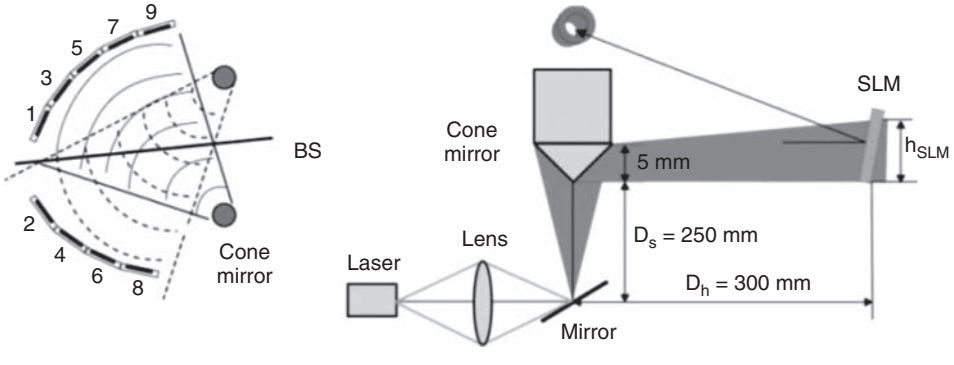

Figure 2.13 Circular holographic display. *Left*, arrangement of the nine phase-only SLMs, denoted as 1 … 9. *Right*, illumination of a single SLM

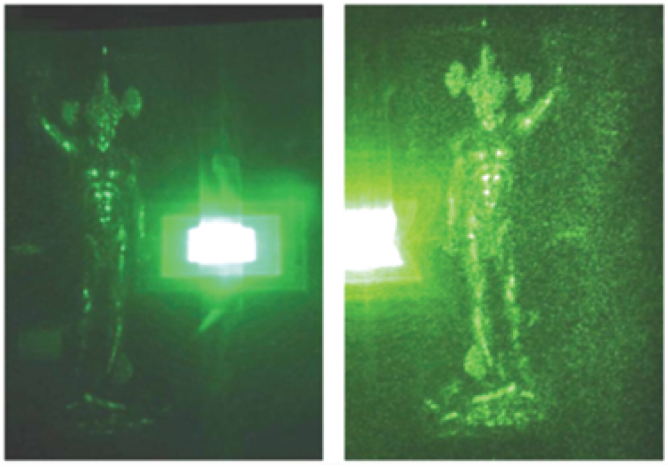

Figure 2.14 *Left*, single SLM optical reconstruction at 0.532 μm of the hologram captured at 10.6 μm and projected on a screen. *Right*, ghostlike multiple SLMs optical reconstruction of the same hologram

2.4.4 Smoke and Flames Hidden Object Holograms

In this section we report the latest results in the field of IRDH at10.6 μm; in particular we illustrate one more useful peculiarity of this technique, which is the possibility to detect objects, or even animate beings, through smoke and, what is even more worthy of note, through a wall of flames. This possibility is a key and challenging target for possible industrial applications and, remarkably, for its possible safety purposes. Visible radiation is strongly affected by smoke or fog, and vision can be completely impaired in smoky environment. On the contrary, the last generation of uncooled IR microbolometer detectors, commercially available for imaging in the thermal infrared, allow passive or active (i.e., with IR laser illumination) clear vision through such scatterers since the IR electromagnetic radiation is just slightly scattered by fog droplets and smoke particles. This property of IR radiation is well known and in fact many fire departments already use these technologies for exploring fire scenarios. Unfortunately, in presence of flames, even these detectors cannot be of great help since the electromagnetic radiation emitted by flames can severely saturate them, as well as standard CCD or CMOS, occluding the scene behind the flames.

As previously discussed, DH at long IR wavelengths has considerable advantages with respect to visible DH, that make it very flexible and useful for recording real world large scenes. Another important characteristic to remark on is the possibility to use only a portion of the acquired hologram to reconstruct the entire scene, even if at the expense of resolution. Finally, DH usually employs a lensless setup to obtain out-of-focus acquisitions and to numerically recover the object wavefield at the desired focus plane in the reconstruction step. All these features, combined with the possibility to exploit IRDH to see behind smoke and flames, provide the unique possibility to perform real-time dynamic detection of moving people in fire scenes, independent of the chemical nature of the burning materials involved and from their emission spectrum. In order to demonstrate these unique imaging potentialities,

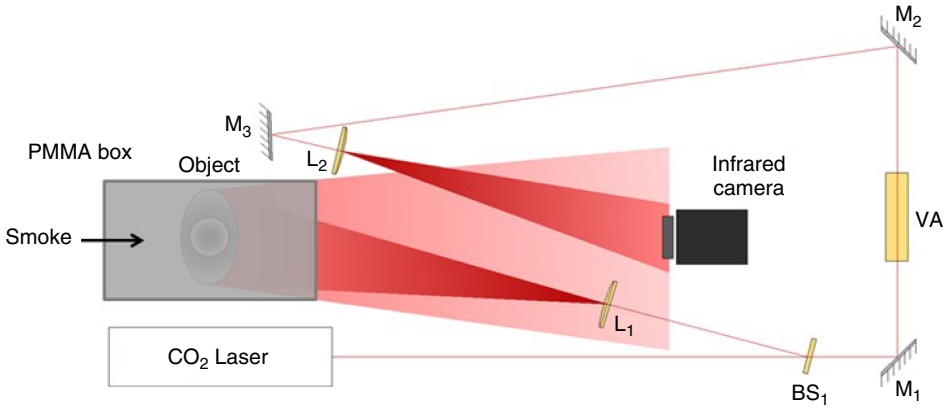

Figure 2.15 Imaging through smoke: employed setup

two kinds of experiments were conducted where the capability of seeing through smoke and flames by IRDH were respectively tested.

In an early series of experiments [31] the capability of IRDH to work efficiently in smoky environments was tested. In order to investigate this condition the basic holographic setup was used but the object under investigation was immersed in a thick blanket of smoke (Fig. 2.15). As a test object the same small Augustus statuette was used but, in order to obtain enough high smoke density around it, it was inserted inside a sealed Polymethyl methacrylate box. In one face of the box two windows in the IR range were fixed: an input AR/AR ZnSe input window through which the laser beam could reach the object and a germanium output window through which the light diffused by the object could reach the thermocamera.

By means of a lateral aperture placed in the box, smoke obtained by burning incense in a small furnace was injected inside the box and a holographic video of the interferometric pattern with the increasing smoke density was recorded. In order to have a quantitative measurement of the smoke concentration inside the box at any moment, the intensity attenuation of a 15 mW laser diode radiation travelling 6 cm inside the box was evaluated. In Fig. 2.16 the visible images of the empty box and after inletting smoke are shown; evidently at high smoke density the vision is completely impaired because of the severe scattering of the visible radiation; at the maximum smoke density the current in the photodiode was reduced by two orders of magnitude and it was impossible to see the statuette, even from the short side of the box.

In Fig. 2.16 the images obtained with the thermocamera, working in normal mode with its IR objective in the two conditions, are also shown. As expected, with a standard thermographic image the object immersed in the smoke is still clearly visible since IR light at such long wavelengths is only slightly scattered by smoke particles. Finally, the reconstructed IR holographic images in the two conditions, shown in Fig. 2.16, demonstrate that clear vision through smoke can be obtained by means of IRDH too.

It is important to note here that the random movements of the scattering particles (smoke and dust particles), which represents a noise source in the standard thermographic image, on the contrary may contribute to getting clearer vision in the holographic reconstruction. Indeed, it has been shown that, if multiple acquisitions are reconstructed and opportunely averaged, better quality images with less noise can be obtained [31].

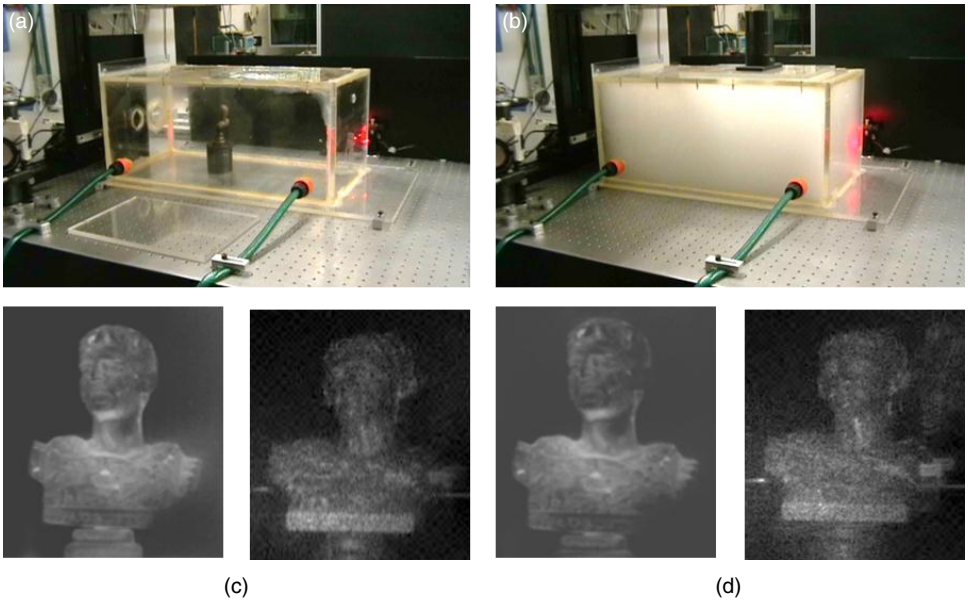

Figure 2.16 (a) Augustus statuette in the box without smoke. (b) Augustus statuette in the box filled with smoke. (c) Box without smoke: thermographic imaging of Augustus on the left and hologram amplitude reconstruction on the right. (d) Box with smoke: thermographic imaging of Augustus on the left and hologram amplitude reconstruction on the right

In a second series of experiments [31] the capability of IRDH to detect an object hidden behind a curtain of flames was tested. In these tests the basic holographic setup with flames inserted between the thermocamera and the object (Fig. 2.17) was used.

The tests were performed employing portable mini stoves to create the wall of flames and a live human half bust as a target. A large portion of the object was covered by flames, impairing vision by means of a common CCD camera. Noteworthy in this case, a clear thermographic vision of the whole scene with no blind areas was impaired as well. On the contrary, the holographic recorded image did not show such a problem, allowing visibility through flames without significant resolution loss. This capability can be explained by the fundamental intrinsic features of holography. First of all, since no objective is required during hologram recording, the IR radiation energy emitted by the flames is not focused on the detector but is distributed over its whole surface; this means that no image of the flames is formed on the detector and, consequently, no pixel saturation effect is obtained. In other words, since out of focus images are recorded in DH, the typical saturation effect of the IR camera elements observed in standard imaging configurations is avoided and the sensor is not blinded by the flame emission. If the radiation energy intercepted by the sensor was so high to disturb the detector somehow, it would be, however, always possible to use a narrow band filter around 10.6 to completely remove its contribution. A second important aspect of the question, strictly related to the interferometric nature of DH technique, is that the flames' radiation is not coherent with the radiation used to get the interferogram and consequently does not affect the interferometric pattern in any way. Furthermore, thanks to the ability of holography to reconstruct

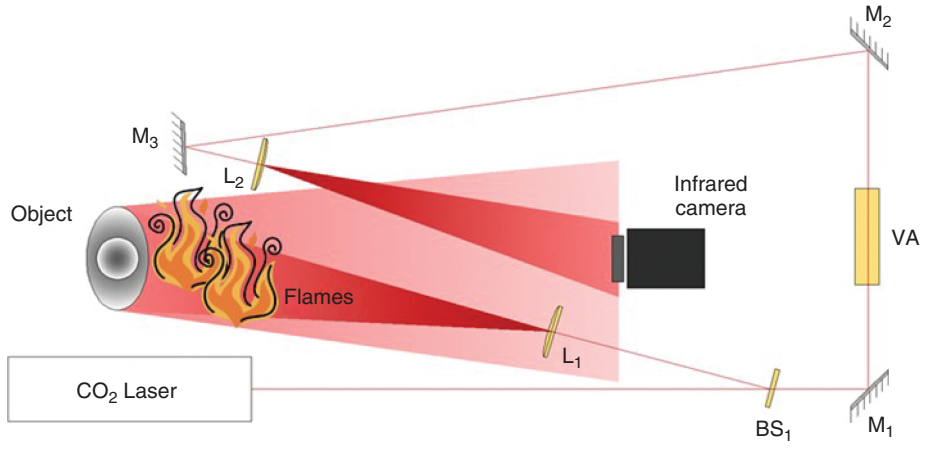

Figure 2.17 Imaging through flames: employed setup

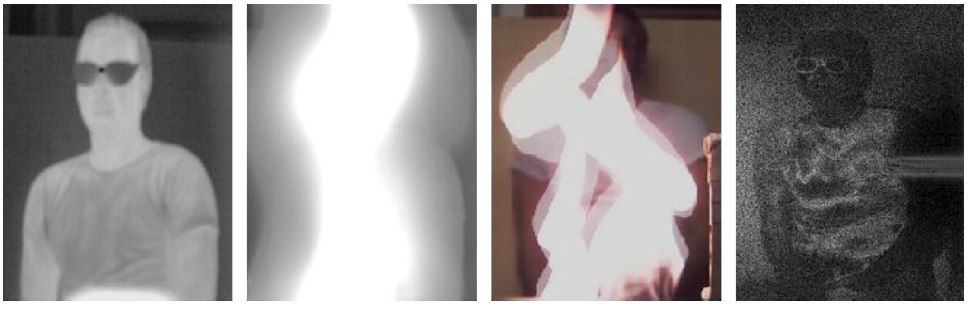

Figure 2.18 Imaging of a live human being seen through flames. From left to right; thermographic image without flames, thermographic image with flames, visible image with flames, holographic reconstructed image with flames

the object wavefront entirely from a smaller portion of the hologram, this technique allows enhanced vision even if some macro-particles, often present in real fire-scenarios, obstruct direct imaging. The advantages of digital holographic image system with respect to standard thermographic and visible recording systems are clearly noticeable in the comparison of the visible, thermal, and holographic reconstructed images in Fig. 2.18.

2.5 Conclusion

As we have seen, IRDH at 10.6 µm has paved the way for large sized object investigation, especially for non-destructive testing and, thanks to its ability to see through smoke, dust particles and flames. It could be employed in the future, to large kinds of applications. Mid-IRDH could also play a very important role in research activity into 3D displays: holographic television,

commonly regarded as the holy grail of holography, is one of the most promising and challenging developments for the future display market. Only holography can provide all depth information necessary to obtain the reconstruction of natural-looking 3D scenes; IRDH, thanks to its capacity to record whole wavefront information of large size samples in daylight and not isolated conditions, and thanks to the possible developments introduced by the progresses of spatial light modulators, may play an important role in this challenge.

References

[1] Gábor D., A new microscopic principle, *Nature* **161**, pp. 777–778 (1948).

[2] Goodman J. W. and Lawrence R. W., Digital image formation from electronically detected holograms, *Applied Physics Letters* **11**, pp. 77–79 (1967).

[3] Schnars U. and Jüptner W. P. O., *Digital Holography, Digital Hologram Recording, Numerical Reconstruction and Related Techniques*, [1st edn], Springer (2005).

[4] Goodman J. W., *Introduction to Fourier Optics*, [2nd edn], McGraw-Hill (1996).

[5] Grilli S., Ferraro P., De Nicola S., Finizio A., Pierattini G., and Meucci R., Whole optical wavefields reconstruction by digital holography, *Optics Express* **9**, pp. 294–302 (2001).

[6] De Nicola S., Ferraro P., Finizio A., and Pierattini G., Correct-image reconstruction in the presence of severe anamorphism by means of digital holography, *Optics Letters* **26**, pp. 974–976 (2001).

[7] De Nicola S., Ferraro P., Finizio A., De Natale P., Grilli S., Pierattini G., and A Mach-Zender interferometric system for measuring the refractive indices of uniaxial crystals, *Optics Communications* **202**, pp. 9–15 (2002).

[8] Ferraro P., De Nicola S., Finizio A., Coppola G., Grilli S., Magro C., and Pierattini G., Compensation of the inherent wave front curvature in digital holographic coherent microscopy for quantitative phase-contrast imaging, *Applied Optics* **42**, pp. 1938–1946 (2003).

[9] De Nicola S., Ferraro P., Finizio A., Grilli S., and Pierattini G., Experimental demonstration of the longitudinal image shift in digital holography, *Optical Engineering* **42**, pp. 1625–1630 (2003).

[10] Grilli S., Ferraro P., Paturzo M., Alfieri D., De Natale P., De Angelis M., *et al*., In-situ visualization, monitoring and analysis of electric field domain reversal process in ferroelectric crystals by digital holography, *Optics Express* **12**, pp. 1832–1834 (2004).

[11] Ferraro P., De Nicola S., Coppola G., Finizio A., Alfieri D., and Pierattini G., Controlling image size as a function of distance and wavelength in Fresnel-transform reconstruction of digital holograms, *Optics Letters* **29**, pp. 854–856 (2004).

[12] De Angelis M., De Nicola S., Finizio A., Pierattini G., Ferraro P., Grilli S., and Paturzo M., Evaluation of the internal field in lithium niobate ferroelectric domains by an interferometric method, *Applied Physics Letters* **85**, pp. 2785–2787 (2004).

[13] Paturzo M., Alfieri G., Grilli S., Ferraro P., De Natale P., De Angelis M., *et al*., Investigation of electric internal field in congruent LiNbO3 by electro-optic effect, *Applied Physics Letters* **85**, pp. 5652–5654 (2004).

[14] De Nicola S., Finizio A., Pierattini G., Alfieri D., Grilli S., Sansone L., and Ferraro P., Recovering correct phase information in multiwavelength digital holographic microscopy by compensation for chromatic aberrations, *Optics Letters* **30**, pp. 2706–2708 (2005).

[15] Ferraro P., Grilli S., Miccio L., Alfieri D., De Nicola S., Finizio A., and Javidi B., Full color 3-D imaging by digital holography and removal of chromatic aberrations, *Journal of Display Technology* **4**, pp. 97–100 (2008).

[16] Merola F., Miccio L., Paturzo M., De Nicola S., and Ferraro P., Full characterization of the photorefractive bright soliton formation process using a digital holographic technique, *Measurement Science & Technology* **20**, 045301 (2009).
[17] Miccio L., Finizio A., Puglisi R., Balduzzi D., Galli A., and Ferraro P., Dynamic DIC by digital holography microscopy for enhancing phase-contrast visualization, *Biomedical Optics Express* **2**, pp. 331–344 (2011).
[18] Paturzo M., Finizio A., and Ferraro P., Simultaneous multiplane imaging in digital holographic microscopy, *Journal of Display Technology* **7**, pp. 24–28 (2011).
[19] Memmolo P., Finizio A., Paturzo M., Miccio L., and Ferraro P., Twin-beams digital holography for 3D tracking and quantitative phase-contrast microscopy in microfluidics, *Optics Express* **19**, pp. 25833–25842 (2011).
[20] Paturzo M., Finizio A., Memmolo P., Puglisi R., Balduzzi D., Galli A., and Ferraro P., Microscopy imaging and quantitative phase contrast mapping in turbid microfluidic channels by digital holography, *Lab Chip* **12**, pp. 3073–3076 (2012).
[21] Bianco V., Paturzo M., Finizio A., Balduzzi D., Puglisi R., Galli A., and Ferraro P., Clear coherent imaging in turbid microfluidics by multiple holographic acquisitions, *Optics Letters* **37**, pp. 4212–4214 (2012).
[22] Bianco V., Paturzo M., Finizio A., Ferraro P., and Memmolo P., seeing through turbid fluids: a new perspective in microfluidics, *Optics and Photonics News* **23**(12), pp. 33–33 (2012).
[23] Bianco V., Paturzo M., Memmolo P., Finizio A., Ferraro P., and Javidi B., Random resampling masks: a non-Bayesian one-shot strategy for noise reduction in digital holography, *Optics Letters* **38**(5), pp. 619–621 (2013).
[24] Born M. and Wolf E., *Principles of Optics, Electromagnetic Theory of Propagation, Interference and Diffraction of Light*, [7th edn (expanse)], Cambridge University Press (1999).
[25] Allaria E., Brugioni S., De Nicola S., Ferraro P., Grilli S., and Meucci R., Digital holography at 10.6 μm, *Optics Communications* **215**, pp. 257–262 (2003).
[26] Pelagotti A., Locatelli M., Geltrude A., Poggi P., Meucci R., Paturzo M., *et al*., Reliability of 3D imaging by digital holography at long IR wavelength, *Journal of Display Technology*, **6**(10), pp. 465–471 (2010).
[27] Pelagotti A., Paturzo M., Geltrude A., Locatelli M., Meucci R., Poggi P., and Ferraro P., Digital holography for 3D imaging and display in the IR range: challenges and opportunities, *3D Research*, **1**(4/06), pp. 1–10 (2010).
[28] Pelagotti A., Paturzo M., Locatelli M., Geltrude A., Meucci R., Finizio A., and Ferraro P., An automatic method for assembling a large synthetic aperture digital hologram, *Optics Express* **20**(5), pp. 4830–4839 (2012).
[29] Maes F., Vandermeulen D., and Suetens P., Medical image registration using mutual information, *Proc IEEE* **91**(10), 1699–1722 (2003).
[30] Geltrude A., Locatelli M., Poggi P., Pelagotti A., Paturzo M., Ferraro P., and Meucci R., Infrared digital holography for large object investigation *Proc. SPIE* 8082–8012 (2011).
[31] Locatelli M., Pugliese E., Paturzo M., Bianco V., Finizio A., Pelagotti A., *et al*., Imaging live humans through smoke and flames using far-infrared digital holography, *Optics Express* **21**(5), pp. 5379–5390 (2013).
[32] Onural L., Yaraş F., and Kang H., Digital holographic three-dimensional video displays, *Proc. IEEE* **99** 576 (2011).
[33] Yaraş F., Kang H., and Onural L., State of the art in holographic displays: A survey, *Journal of Display Technology* **6**(10), 443–454 (2010).
[34] Meier R. W., Magnification and third-order aberrations in holography, *Journal of the Optical Society of America* **55**(8), 987–992 (1965).

[35] Paturzo M., Pelagotti A., Finizio A., Miccio L., Locatelli M., Geltrude A., *et al*., Optical reconstruction of digital holograms recorded at 10.6 μm: route for 3D imaging at long infrared wavelengths, *Optics Letters* **35**(12), pp. 2112–2114, (2010).

[36] Stoykova E., Yaraş F., Kang H., Onural L., Geltrude A., Locatelli M., *et al*., Visible reconstruction by a circular holographic display from digital holograms recorded under infrared illumination, *Optics Letters* **37**(15), pp. 3120–3122 (2012).

[37] Yaraş F., Kang H., and Onural L., Circular holographic video display system, *Optics Express* **19**(10), 9147–9156 (2011).